# Dynamical Control of Topology in Polar Skyrmions via Twisted Light

Lingyuan Gao, Sergei Prokhorenko, Yousra Nahas, and Laurent Bellaiche

# Dynamical control of topology in ferroelectric skyrmions
# via twisted light

Lingyuan Gao,[1] Sergei Prokhorenko,[1] Yousra Nahas,[1] and Laurent Bellaiche[1, *]

[1]*Physics Department and Institute for Nanoscience and Engineering,*
*University of Arkansas, Fayetteville, Arkansas, 72701, USA*
(Dated: November 13, 2023)

Twisted light carries a non-zero orbital angular momentum, that can be transferred from light to electrons and particles ranging from nanometers to micrometers. Up to now, the interplay between twisted light with dipolar systems has scarcely been explored, though the latter bear abundant forms of topologies such as skyrmions and embrace strong light-matter coupling. Here, using first-principles-based simulations, we show that twisted light can excite and drive dynamical polar skyrmions and transfer its nonzero winding number to ferroelectric ultrathin films. The skyrmion is successively created and annihilated alternately at the two interfaces, and experiences a periodic transition from a markedly "Bloch" to "Néel" character, accompanied with the emergence of a "Bloch point" topological defect with vanishing polarization. The dynamical evolution of skyrmions is connected to a constant jump of topological number between "0" and "1" over time. These intriguing phenomena are found to have an electrostatic origin. Our study thus demonstrates that, and explains why, this unique light-matter interaction can be very powerful in creating and manipulating topological solitons in functional materials.

With their noncolinear spin patterns and particle-like features [1, 2], skyrmions have attracted enormous interests in condensed matter physics. Their unique properties, such as topological Hall effect [3, 4] and low current-driven motion [5, 6], enable promising applications, including racetrack memory and logic gates [7–10]. Inspired by these discoveries, scientists recently aimed to seek an electric counterpart of topological solitons in ferroelectric systems, as they can be more easily controlled by electric field [11–13]. Polar patterns with skyrmion topologies have been predicted in $BaTiO_3/SrTiO_3$ nanocomposites and bulk $PbTiO_3$ by first-principles-based approaches [14, 15], and lately skyrmion-like polar solitons have been observed in $(PbTiO_3)_n/(SrTiO_3)_n$ superlattices and $SrTiO_3/Pb(Zr_xTi_{1-x})O_3/SrTiO_3$ heterostructures [16–18]. Different from magnetic skyrmions forming out of asymmetric exchange interaction between spins [19, 20], nontrivial ferroelectric structures typically originate from a competition between elastic, electrostatic and gradient energies [14, 21].

In addition to magnetic spins and electric dipoles, skyrmion can also be constructed from other three-dimensional vector fields. By controlling the interference of plasma polaritons on a patterned metallic plate, the optical skyrmion lattice can be established from evanescent electromagnetic waves [22, 23]. Unlike static magnetic and polar skyrmions, optical skyrmions display a dynamical characteristic due to the nature of electromagnetic fields. By using time-resolved photoemission electron microscopy, it is observed that the field configuration of Néel skyrmions evolves over time in a repetitive pattern marked by the continuous reversal of the out-of-plane components, resulting in a periodic modulation of the skyrmion number [24]. Such spatial-temporal variations of vector fields, which provide valuable insights into skyrmion dynamics, are rarely seen in other media, including both magnetic and ferroelectric materials.

In this work, we present a promising approach to induce dynamical polar skyrmions at interfacial layers in ferroelectric $Pb(Zr_xTi_{1-x})O_3$ (PZT) ultrathin films, allowing such topological defects to evolve in a controllable manner. By introducing interaction between electric dipoles and external nontrivial light, dipoles form a skyrmion and it dynamically evolves between a markedly "Bloch-"type to "Néel-"type, as a transient electrodynamic response to the optical field. A topological defect "Bloch point" with vanishing polarization is identified for the first time in ferroelectrics and is involved in skyrmion creation [25, 26]. Moreover, the robustness of the mechanism manifests itself in the sense that the skyrmion is well maintained under different conditions, and its intrinsic characteristics such as size and switching speed are highly tunable by controlling external variables of the beam. Our study thus shows that the ferroelectric system can serve as a promising platform for presenting polar patterns that exhibit dynamical characters via light-matter interaction.

The optical field we introduce into the PZT ultrathin films is called optical vortex (OV) beam, which is akin to superfluid vortices and carries a non-zero orbital angular momentum (OAM) [27–29]. In recent works, nonuniform heating and magnetic field in the form of a vortex beam have been predicted to induce topological defects in chiral magnets [30, 31]. Here, we explore whether the nontrivial optical field can be printed on dipoles to create topological solitons in ferroelectric systems.

Technically, we use a first-principles-based effective Hamiltonian approach to study ferroelectric ultrathin films made of $Pb(Zr_{0.4}Ti_{0.6})O_3$ (PZT) [32–34]. Under different mechanical and electrical conditions, PZT and

related systems have been found to exhibit several exotic phases, including vortex [35], flux-closure [36], and nanobubble domains [37]. Here, we introduce the lowest order of the "Laguerre-Gaussian" beam (i.e., $l = 0$) propagating along the direction normal to the film and passing through the center of each (001) layer to interact with the well-equilibrated monodomain at 10 K (**Fig. 1**) [27]. As such, the time-dependent, in-plane electric field can be written as:

$$\vec{E}(\vec{r}, t) = E_0 \left(\frac{\sqrt{2}\rho}{w}\right)^{|m|} e^{-\frac{\rho^2}{w^2}}$$
$$\left( \cos{(m\phi - \omega t)} \vec{e}_x - \sigma \sin{(m\phi - \omega t)} \vec{e}_y \right). \qquad (1)$$

Here, $\vec{e}_x$ and $\vec{e}_y$ are polarization vectors along the $x$- and $y$-axes that are lying along the [100] and [010] pseudo-cubic (p.c.) directions, respectively; $m\phi$ and $\sigma$ characterize the phase twist of the field and the handness of the polarization, corresponding to orbital and spin angular momentum, respectively; $E_0$, $\omega$ and $w$ denote the field magnitude, light frequency and beam radius, respectively. $\vec{r}$ ($\rho$, $\phi$, $z$) is the position vector from the center of the supercell to any B-site of the film in cylindrical coordinates. In the present work, we set $\omega = 1$ THz, $w = 5$ unit cells (u.c.), and we consider $\sigma = 1, m = -1$ for simplicity; as such, this electric field $\vec{E}$ always has an in-plane orientation and carries a winding number $w_v[\vec{E}] = -m$ [38]. The characteristic time of polarization switching $\tau$ can be estimated from the kinetic energy and the leading self-energy of local mode (see Supplementary Material [39]), and $\tau \approx 0.1$ ps falls in the range of the variation of a THz electric field. Computational details about other parameters and justifications for choosing their values are detailed in the Supplementary Material.
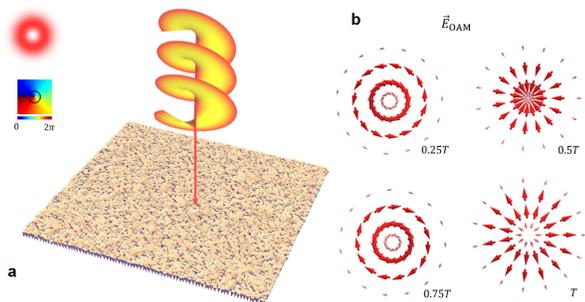


FIG. 1. **Illumination of poled PZT films by an OV beam**. **a** The helical wavefront represents the OV beam. The red "doughnut" shape in the upper left corner denotes the circularly-symmetric intensity profile of the $l = 0$ and $m = 1$ "Laguerre-Gaussian" mode, and the colorful palette shows its phase variation of $2\pi$. Local electric dipoles are represented by cones pointing down. **b** The evolution of the beam-generated electric fields within the film. The four panels show subsequent field configurations (anti-clockwise, convergent, clockwise and divergent vortices) separated by quarter of a period $T$.

We turn on the OAM field at $t = 0$. Molecular dynamics simulations show that at the time $t = 3$ ps, the local dipoles already establish a well defined cyclical motion passing through a sequence of states shown in **Fig. 2a-b**. Each of such states has a continuous rotational symmetry around the central line of the vortex beam. Hence, in the subpanels of **Fig. 2a** we show the distribution of dipoles only in one of the radial cross sections, i.e., the $y = 40$ ($x, z$) plane passing through the rotational symmetry axis. Technically, the slab used to model our PZT films have eight (001) layers, including one for the substrate (layer 1), five for the film (layers 2-6), and two for the vacuum (layers 7 and 8). Additionally, we schematically show in **Figs. 2a1, b1** the structural evolution of the dipoles in the top and bottom ($x, y$) planes of the film (further plots showing the time evolution of dipole configurations at these two planes are reported in Fig. S2).

At $t = 3.3$ ps (**Fig. 2a**) the polar structure is homogeneous throughout all layers. The dipoles both at the center of the beam ($\rho = 0$) and in the far-field region ($\rho > 13$ u.c.) retain their original downward orientation. In contrast, at the intermediate distances from the central line ($1 < \rho < 10$ u.c.), the out-of-plane component ($P_z$) of electric dipoles is suppressed. Within this ring-shaped region, the in-plane components $P_x$ and $P_y$ grow following the intensity profile of the beam (**Fig. 1a**) and form an anti-clockwise vortex pattern (see the $0.25T$ field configuration in **Fig. 1b**) where $T$ denotes the period of the field. The rotations from the out-of-plane to in-plane orientations have a pronounced Bloch character as illustrated in the top leftmost panel of **Fig. 2a**. Overall, the structure at $t = 3.3$ ps can be described as an anti-clockwise annular vortex with downwards polarized core and surrounded by a downwards polarized matrix.

As time passes, the downwards polarized core ($\rho = 0$) rapidly undergoes a partial switching. For instance, at $t = 3.4$ps the direction of the central dipole in top plane ($z = 6$) is already reversed to $P_z > 0$. At the same time, the core dipoles in all other planes are still oriented downwards but their magnitude decreases with increasing $z$. Such inhomogeneous core structure persists from $t \approx 3.38$ps up to $t \approx 3.75$ps, i.e., during almost a full half period. It is also important to note that owing to the gradient of $P_z$ at $\rho = 0$, the magnitude of the central dipole in the $z = 5$ plane almost vanishes at $t = 3.5$ps and $t = 3.6$ps. As will be discussed later, such quasi-singular behavior as well as the reversal of $P_z$ at the top layer are non-trivial topological features. Note, however, that all layers possess similar patterns for the in-plane dipole components $P_x$ and $P_y$ at any given time (see Fig. S1).

Another structural change that occurs during the first half-period is the rotation of the dipoles around the $z$-axis (top row in **Fig. 2a**) which is remindful of the evolution of the OAM field (**Fig. 1b**). Such rotation
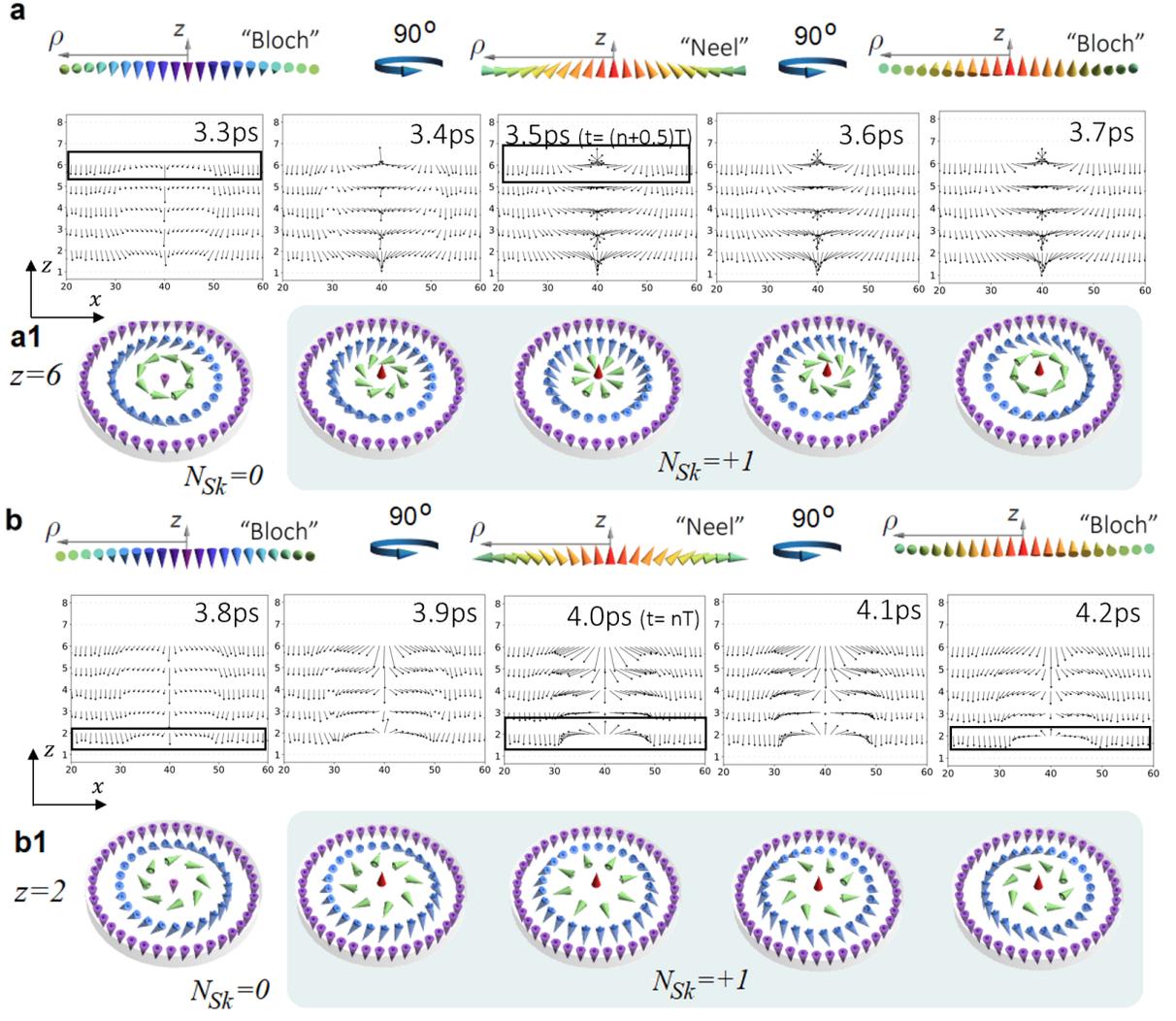
FIG. 2. **Effective Hamiltonian simulation of the electric dipole evolution in the presence of an OAM field**. **a**. The view of the dipole configuration in the $y = 40$ plane in the first-half period $(3.3 - 3.7\text{ps})$, containing $P_x$ and $P_z$ (denoted by black arrows). The horizontal axis denotes the site number along the [100] direction and the vertical axis denotes the index of the (001) layers. Top row illustrates the "Bloch"→"Néel"→"Bloch" rotations of the dipoles at the top layer $(z = 6)$ highlighted by the black box. **a1**. Schematic plot about the dynamical skyrmion evolution at the top interfacial layer during the first half period $(3.3 - 3.7\text{ps})$. **b**. Similar to **a**, the view of the dipole configuration in the $y = 40$ plane in the second-half period $(3.8 - 4.2\text{ps})$. Top row illustrates the "Bloch"→"Néel"→"Bloch" rotations of the dipoles at the bottom layer $(z = 2)$ highlighted by the black box. **b1**. Schematic plot about the dynamical skyrmion evolution at the bottom interfacial layer during the second half period $(3.8 - 4.2\text{ps})$.

gradually transforms the dominant Bloch component at $t = 3.3\text{ps}$ into its center-convergent Néel counterpart at $t = 3.5 - 3.6\text{ps}$ until, having accomplished a 180° turn, the dipolar structure re-gains its assertive Bloch character at $t = 3.7\text{ps}$, but is reversed with respect to $t = 3.3\text{ps}$ (rightmost vs leftmost top panel in **Fig. 2a**).

Thereby, the first half-period ends at $t = 3.8\text{ps}$ with an annular vortex state akin to the $t = 3.3\text{ps}$ structure but in a clock-wise manner. During the second half-period $t = 3.8 - 4.2\text{ps}$ (**Fig. 2b**), dipoles at each site continue to rotate anti-clockwise around the $z-$axis. Such rotations generate the center-divergent (e.g., $t = 4.0\text{ps}$) and the

anti-clockwise (e.g., $t = 4.2\text{ps}$) vortex patterns in the $(x,y)$ planes. The corresponding mutual transformation of Bloch and Néel rotations are schematically shown in the top row of **Fig. 2b**. Moreover, similar to the first-half-period evolution, the core polarization is partially switched during $t = 3.88 - 4.25\text{ps}$. Yet, the reversal of $P_z$ is rather observed in the bottom $(z = 2)$ plane of the film, while in all other planes the magnitude of $P_z$ increases with $z$. Consequently, the quasi-singular point $(\mathbf{P} \approx 0)$ occurs in the $z = 3$ plane.

One can readily notice (**Figs. 2a1, b1**) that the optical vortex creates polar skyrmion textures at the top and

bottom interfaces of the film whenever the direction of the central dipole in the corresponding layers is reversed. This observation is confirmed by the calculated evolution of the skyrmion number $N_{\text{Sk}}$ for $z = 2 - 6$ planes (**Fig. 3a**). As the in-plane dipole components closely follow the morphology of the OAM field, the skyrmion helicity $\gamma$ also continuously evolves with time accompanying the vortex beam's phase, i.e., $\gamma = \omega t \,(\text{mod}\, 2\pi)$ [1]. For instance, a perfectly center-divergent (convergent) Néel skyrmion characterized by $\gamma = 0$ ($\gamma = \pi$) forms at $t = T$ ($t = 0.5T$) on the bottom (top) interface; in contrast, at the same time, center-divergent(convergent) skyrmions never occur at the top (bottom) plane (**Figs. 2a1, b1**). Additionally, at $t = 0.25T$ or $t = 0.75T$ ($\gamma = \pm\pi/2$), the system always opts for a topologically trivial annular vortex state instead of Bloch skyrmions. Since the dipoles forming the skyrmion texture have to cover the full body angle, such behavior is topologically tied to the inhomogeneous switching of $P_z$ at the center line.

Interestingly, such switching is not a direct effect of the beam-generated field since $\vec{E}(\vec{r}, t)$ lacks an out-of-plane component at all times, but also vanishes at $\rho = 0$. Instead, the switching mechanism roots in the electrostatic interactions between $P_{x,y}$ and $P_z$. Namely, the development of the radial component of polarization leads to a build-up of an electric bound charge $\rho_b^{x,y} = -(\partial_x P_x + \partial_y P_y)$. In response, by adopting a monotonically changing $P_z(z)$, the material develops a bound charge $\rho_b^z = -\partial_z P_z$ to compensate $\rho_b^{x,y}$ (illustrated in **Fig. 3b**). Such mechanism is further confirmed by our calculations of bound charges $\rho_b^z$ and $\rho_b^{x,y}$ evolving with time (see Supplementary Material). Thereby, depending on the sign and magnitude of $\rho_b^{x,y}$, the reversal of $P_z$ occurs either in the vicinity of the top or bottom interfaces whenever $d \gtrsim |P_z^{\text{max}}|/|\rho_b^z|$, where $d$ denotes the film thickness. On interfacial layers, the continuity condition is naturally removed, so polarization there can have more abrupt change compared to polarization at layers far from the interface. This condition also defines the minimum values of parameters (i.e., field magnitude $E_0$ and film thickness $d$) required to create polar skyrmion textures by the OAM light (see Supplementary Material). We also expect that it is more difficult to induce a dynamical polar skyrmion in a much thicker PZT film, where the response of electric polarization and bound charge to the external electric field gets weaker due to a stronger dielectric screening and a weaker surface depolarization field in a 3D-like system.

The evolution of $P_z$ and $\rho_b$ with time also allows to explain the formation of polar skyrmions from a topological perspective. Specifically, the continuity of polarization does not allow $N_{\text{sk}}$ to vary with time, unless a topological transition occurs. This can be realized by introducing a Bloch point, a three-dimensional singularity with vanishing polarization. Such defect has been seen to mediate the dynamical evolution of magnetic skyrmions [40]. As

being composed of planes with different $N_{\text{sk}}$, Bloch point can induce a jump of $N_{\text{sk}}$ by 1 when going through these planes. Above discussion about **Fig. 2** points out a negligible dipole moment at the center of layer 3 or layer 5 when skyrmion is present. Indeed, with the same method used in Ref. [26], by computing the topological charge of each cell, we find a negatively charged (-1) Bloch point at the center between layer 2 and layer 3 during 3.9–4.2 ps, and a positively charged (+1) Bloch point at the center between layer 5 and layer 6 during 3.4–3.7 ps, in concert with the presence of a skyrmion. According to **Fig. 2**, both Bloch points have spiraling configurations evolving with time as schematically shown in **Fig. 3c**, and they are involved in the creation of polar skyrmions. Note at 3.5 ps and 3.7 ps (4.0 ps and 4.1 ps), the dipole at the center of layer 5 (layer 3) exhibits extremely small magnitudes, indicating the singularity feature of a Bloch point; while at 3.4 ps and 3.6 ps (3.9 ps and 4.2 ps), the dipoles there has a more notable magnitude, and the exact position of a Bloch point can be determined by interpolating dipoles at the center of adjacent layers along z directions.

We note $N_{\text{sk}}$ of the two interfacial layers stay on "0" and "1" alternately. This behavior keeps proceeding as long as the OAM field does not vanish (Fig. S7). The interconversion between $N_{\text{sk}}$ of "0" or "1" highly resembles digital binary signals and suggests that this dynamical skyrmion can be implemented as a component in logic gates. The variation of the skyrmion number also bears resemblance to that of optical skyrmion constructed from surface plasmon polariton [22, 24], owing to its transient nature that dipoles adjust their alignments instantly to the incident OAM field. Though $N_{\text{sk}}$ cannot be directly observed, it is associated with the switching of out-of-plane dipole components. This can be probed by measuring the out-of-plane polarization $P_z$ using interdigited electrodes [12]. **Figure 3d** shows how $P_z$ averaged within the skyrmion radius at each (001) layer changes with time. With periodic evolution of dipole components, we see that when the corresponding Néel-type skyrmion is formed, $P_z$ at layer 2 or layer 6 reach its maxima and has positive values, in contrast to negative values at most other times. By tuning the magnitude of the OAM field $E_0$, as well as thickness of the film and its screening to the depolarization field, the positive $P_z$ value can be further increased, resulting in a more prominent detection signal (see Figs. S5, S6, S9). The sub-picosecond period represents a much faster switching process, as compared to conventional memory devices ($\mu$s) and magnetic skrymions (ns) [41]. Furthermore, the switching period of $N_{\text{sk}}$ can be tuned by the frequency of the field (Fig. S8). As we vary the field magnitude and the screening of the depolarization field, the skyrmions are stabilized when parameters span a large range (Fig. S5 and Fig. S9). Moreover, by delicately tuning the electrostatic energy, namely, starting from a stripe phase, the lifetime of the dynamical skyrmion can be extended: the dynamical
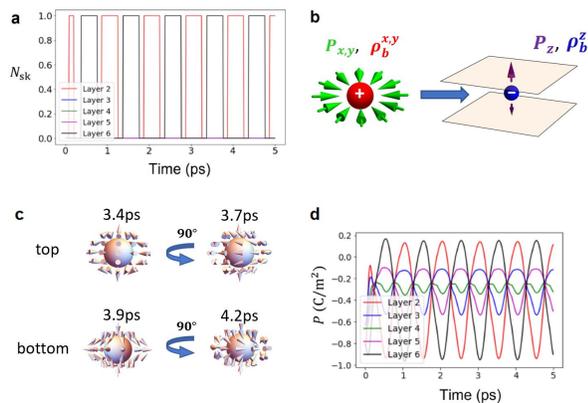
FIG. 3. **Topological and electrostatic origin of the OAM-induced-skyrmion**. **a** The variation of skyrmion number $N_{sk}$ at each layer with time. **b** Illustration about bound charge density $\rho_b^{x,y}$ induced by $P_{x,y}$, and $\rho_b^z$ induced by $P_z$ to compensate $\rho_b^{x,y}$. **c** Illustration about two spiraling Bloch points located between layer 5 and layer 6 (first half period) and between layer 2 and layer 3 (second half period). 90 degree denotes dipole evolution with time. **d** The variation of averaged $P_z$ within skyrmion radius at each layer with time.

skyrmion survives even when the field is much lower than the minimal threshold magnitude, and it evolves into a stable skyrmion even after the field is removed (see Supplementary Material and Fig. S9).

In summary, we predict that the nontrivial winding pattern of the field in an optical vortex beam can be imprinted in ferroelectrics, and dipolar skyrmions will emerge and evolve dynamically out of an electrostatic cooperation between microscopic bound charges and external field. This unusual light-matter interaction delivers a new perspective about dynamically manipulating topological solitons in ferroelectric materials.

* laurent@uark.edu

[1] N. Nagaosa and Y. Tokura, Topological properties and dynamics of magnetic skyrmions, Nature nanotechnology **8**, 899 (2013).

[2] A. Fert, N. Reyren, and V. Cros, Magnetic skyrmions: advances in physics and potential applications, Nature Reviews Materials **2**, 1 (2017).

[3] A. Neubauer, C. Pfleiderer, B. Binz, A. Rosch, R. Ritz, P. Niklowitz, and P. Böni, Topological hall effect in the a phase of mnsi, Physical review letters **102**, 186602 (2009).

[4] Y. Li, N. Kanazawa, X. Yu, A. Tsukazaki, M. Kawasaki, M. Ichikawa, X. Jin, F. Kagawa, and Y. Tokura, Robust formation of skyrmions and topological hall effect anomaly in epitaxial thin films of mnsi, Physical review letters **110**, 117202 (2013).

[5] W. Jiang, P. Upadhyaya, W. Zhang, G. Yu, M. B. Jungfleisch, F. Y. Fradin, J. E. Pearson, Y. Tserkovnyak, K. L. Wang, O. Heinonen, *et al.*, Blowing magnetic skyrmion bubbles, Science **349**, 283 (2015).

[6] S. Woo, K. Litzius, B. Krüger, M.-Y. Im, L. Caretta, K. Richter, M. Mann, A. Krone, R. M. Reeve, M. Weigand, *et al.*, Observation of room-temperature magnetic skyrmions and their current-driven dynamics in ultrathin metallic ferromagnets, Nature materials **15**, 501 (2016).

[7] S. S. Parkin, M. Hayashi, and L. Thomas, Magnetic domain-wall racetrack memory, Science **320**, 190 (2008).

[8] A. Fert, V. Cros, and J. Sampaio, Skyrmions on the track, Nature nanotechnology **8**, 152 (2013).

[9] X. Zhang, M. Ezawa, and Y. Zhou, Magnetic skyrmion logic gates: conversion, duplication and merging of skyrmions, Scientific reports **5**, 1 (2015).

[10] S. Parkin and S.-H. Yang, Memory on the racetrack, Nature nanotechnology **10**, 195 (2015).

[11] L. Wang, Q. Feng, Y. Kim, R. Kim, K. H. Lee, S. D. Pollard, Y. J. Shin, H. Zhou, W. Peng, D. Lee, *et al.*, Ferroelectrically tunable magnetic skyrmions in ultrathin oxide heterostructures, Nature materials **17**, 1087 (2018).

[12] P. Behera, M. A. May, F. Gómez-Ortiz, S. Susarla, S. Das, C. T. Nelson, L. Caretta, S.-L. Hsu, M. R. McCarter, B. H. Savitzky, *et al.*, Electric field control of chirality, Science advances **8**, eabj8030 (2022).

[13] R. Zhu, Z. Jiang, X. Zhang, X. Zhong, C. Tan, M. Liu, Y. Sun, X. Li, R. Qi, K. Qu, *et al.*, Dynamics of polar skyrmion bubbles under electric fields, Physical Review Letters **129**, 107601 (2022).

[14] Y. Nahas, S. Prokhorenko, L. Louis, Z. Gui, I. Kornev, and L. Bellaiche, Discovery of stable skyrmionic state in ferroelectric nanocomposites, Nature communications **6**, 1 (2015).

[15] M. Gonçalves, C. Escorihuela-Sayalero, P. García-Fernández, J. Junquera, and J. Íñiguez, Theoretical guidelines to create and tune electric skyrmions, arXiv preprint arXiv:1806.01617 (2018).

[16] S. Das, Y. Tang, Z. Hong, M. Gonçalves, M. McCarter, C. Klewe, K. Nguyen, F. Gómez-Ortiz, P. Shafer, E. Arenholz, *et al.*, Observation of room-temperature polar skyrmions, Nature **568**, 368 (2019).

[17] Y. Nahas, S. Prokhorenko, Q. Zhang, V. Govinden, N. Valanoor, and L. Bellaiche, Topology and control of self-assembled domain patterns in low-dimensional ferroelectrics, Nature communications **11**, 1 (2020).

[18] L. Han, C. Addiego, S. Prokhorenko, M. Wang, H. Fu, Y. Nahas, X. Yan, S. Cai, T. Wei, Y. Fang, *et al.*, High-density switchable skyrmion-like polar nanodomains integrated on silicon, Nature **603**, 63 (2022).

[19] I. Dzyaloshinsky, A thermodynamic theory of "weak" ferromagnetism of antiferromagnetics, Journal of physics and chemistry of solids **4**, 241 (1958).

[20] T. Moriya, Anisotropic superexchange interaction and

weak ferromagnetism, Physical review **120**, 91 (1960).

[21] A. Yadav, C. Nelson, S. Hsu, Z. Hong, J. Clarkson, C. Schlepütz, A. Damodaran, P. Shafer, E. Arenholz, L. Dedon, *et al.*, Observation of polar vortices in oxide superlattices, Nature **530**, 198 (2016).

[22] S. Tsesses, E. Ostrovsky, K. Cohen, B. Gjonaj, N. Lindner, and G. Bartal, Optical skyrmion lattice in evanescent electromagnetic fields, Science **361**, 993 (2018).

[23] L. Du, A. Yang, A. V. Zayats, and X. Yuan, Deep-subwavelength features of photonic skyrmions in a confined electromagnetic field with orbital angular momentum, Nature Physics **15**, 650 (2019).

[24] T. J. Davis, D. Janoschka, P. Dreher, B. Frank, F.-J. Meyer zu Heringdorf, and H. Giessen, Ultrafast vector imaging of plasmonic skyrmion dynamics with deep subwavelength resolution, Science **368**, eaba6415 (2020).

[25] E. Feldtkeller, Mikromagnetisch stetige und unstetige magnetisierungskonfigurationen, Zeitschrift fur Angewandte Physik **19**, 530 (1965).

[26] A. Thiaville, J. M. García, J. Miltat, T. Schrefl, *et al.*, Micromagnetic study of bloch-point-mediated vortex core reversal, Physical Review B **67**, 094410 (2003).

[27] L. Allen, M. W. Beijersbergen, R. Spreeuw, and J. Woerdman, Orbital angular momentum of light and the transformation of laguerre-gaussian laser modes, Physical review A **45**, 8185 (1992).

[28] Y. Shen, X. Wang, Z. Xie, C. Min, X. Fu, Q. Liu, M. Gong, and X. Yuan, Optical vortices 30 years on: Oam manipulation from topological charge to multiple singularities, Light: Science & Applications **8**, 1 (2019).

[29] G. F. Q. Rosen, P. I. Tamborenea, and T. Kuhn, Interplay between optical vortices and condensed matter, Reviews of Modern Physics **94**, 035003 (2022).

[30] H. Fujita and M. Sato, Ultrafast generation of skyrmionic defects with vortex beams: Printing laser profiles on magnets, Physical Review B **95**, 054421 (2017).

[31] H. Fujita and M. Sato, Encoding orbital angular momentum of light in magnets, Physical Review B **96**, 060407 (2017).

[32] I. Kornev, H. Fu, and L. Bellaiche, Ultrathin films of ferroelectric solid solutions under a residual depolarizing field, Physical review letters **93**, 196104 (2004).

[33] I. Ponomareva, I. Naumov, I. Kornev, H. Fu, and L. Bellaiche, Atomistic treatment of depolarizing energy and field in ferroelectric nanostructures, Physical Review B **72**, 140102 (2005).

[34] I. Ponomareva, I. Naumov, and L. Bellaiche, Low-dimensional ferroelectrics under different electrical and mechanical boundary conditions: Atomistic simulations, Physical Review B **72**, 214118 (2005).

[35] A. Gruverman, D. Wu, H. Fan, I. Vrejoiu, M. Alexe, R. Harrison, and J. Scott, Vortex ferroelectric domains, Journal of Physics: Condensed Matter **20**, 342201 (2008).

[36] Y. Tang, Y. Zhu, X. Ma, A. Y. Borisevich, A. N. Morozovska, E. A. Eliseev, W. Wang, Y. Wang, Y. Xu, Z. Zhang, *et al.*, Observation of a periodic array of flux-closure quadrants in strained ferroelectric pbTiO$_3$ films, Science **348**, 547 (2015).

[37] Q. Zhang, L. Xie, G. Liu, S. Prokhorenko, Y. Nahas, X. Pan, L. Bellaiche, A. Gruverman, and N. Valanoor, Nanoscale bubble domains and topological transitions in ultrathin ferroelectric films, Advanced Materials **29**, 1702375 (2017).

[38] K. Shintani, K. Taguchi, Y. Tanaka, and Y. Kawaguchi, Spin and charge transport induced by a twisted light beam on the surface of a topological insulator, Physical Review B **93**, 195415 (2016).

[39] See Supplemental Material [url] for computational details and methods, origins of skyrmion formation, and critical conditions and robustness of polar skyrmions, which includes Refs. [42–98].

[40] Y. Zhou, E. Iacocca, A. A. Awad, R. K. Dumas, F. Zhang, H. B. Braun, and J. Åkerman, Dynamically stabilized magnetic skyrmions, Nature communications **6**, 1 (2015).

[41] S. Luo and L. You, Skyrmion devices for memory and logic applications, APL Materials **9**, 050901 (2021).

[42] W. Zhong, D. Vanderbilt, and K. Rabe, Phase transitions in BaTiO$_3$ from first principles, Physical Review Letters **73**, 1861 (1994).

[43] W. Zhong, D. Vanderbilt, and K. Rabe, First-principles theory of ferroelectric phase transitions for perovskites: The case of BaTiO$_3$, Physical Review B **52**, 6301 (1995).

[44] L. Bellaiche, A. García, and D. Vanderbilt, Finite-temperature properties of Pb(Zr$_{1-x}$Ti$_x$)O$_3$ alloys from first principles, Physical Review Letters **84**, 5427 (2000).

[45] L. Bellaiche, A. García, and D. Vanderbilt, Low-temperature properties of Pb(Zr$_{1-x}$Ti$_x$)O$_3$ solid solutions near the morphotropic phase boundary, Ferroelectrics **266**, 41 (2002).

[46] L. Nordheim, Zur elektronentheorie der metalle. i, Annalen der Physik **401**, 607 (1931).

[47] L. Bellaiche and D. Vanderbilt, Virtual crystal approximation revisited: Application to dielectric and piezoelectric properties of perovskites, Physical Review B **61**, 7877 (2000).

[48] N. J. Ramer and A. M. Rappe, Application of a new virtual crystal approach for the study of disordered perovskites, Journal of Physics and Chemistry of Solids **61**, 315 (2000).

[49] D. Vanderbilt, Soft self-consistent pseudopotentials in a generalized eigenvalue formalism, Physical review B **41**, 7892 (1990).

[50] P. Hohenberg and W. Kohn, Inhomogeneous electron gas, Physical review **136**, B864 (1964).

[51] A. Garcia and D. Vanderbilt, Electromechanical behavior of BaTiO$_3$ from first principles, Applied Physics Letters **72**, 2981 (1998).

[52] L. Bellaiche, A. García, and D. Vanderbilt, Electric-field induced polarization paths in Pb(Zr$_{1-x}$Ti$_x$)O$_3$ alloys, Physical Review B **64**, 060103 (2001).

[53] B.-K. Lai, I. Ponomareva, I. Naumov, I. Kornev, H. Fu, L. Bellaiche, and G. Salamo, Electric-field-induced domain evolution in ferroelectric ultrathin films, Physical review letters **96**, 137602 (2006).

[54] B.-K. Lai, I. Ponomareva, I. Kornev, L. Bellaiche, and G. Salamo, Thickness dependency of 180° stripe domains in ferroelectric ultrathin films: A first-principles-based study, Applied Physics Letters **91**, 152909 (2007).

[55] S. t. Streiffer, J. Eastman, D. Fong, C. Thompson, A. Munkholm, M. R. Murty, O. Auciello, G. Bai, and G. Stephenson, Observation of nanoscale 180° stripe domains in ferroelectric PbTiO$_3$ thin films, Physical review letters **89**, 067601 (2002).

[56] A. Schilling, T. Adams, R. Bowman, J. Gregg, G. Catalan, and J. Scott, Scaling of domain periodicity with thickness measured in BaTiO$_3$ single crystal lamellae and comparison with other ferroics, Physical Review B **74**,

024115 (2006).

[57] Y. Nahas, S. Prokhorenko, J. Fischer, B. Xu, C. Carrétéro, S. Prosandeev, M. Bibes, S. Fusil, B. Dkhil, V. Garcia, *et al.*, Inverse transition of labyrinthine domain patterns in ferroelectric thin films, Nature **577**, 47 (2020).

[58] I. I. Naumov, L. Bellaiche, and H. Fu, Unusual phase transitions in ferroelectric nanodisks and nanorods, Nature **432**, 737 (2004).

[59] D. Sichuga and L. Bellaiche, Epitaxial $Pb(Zr,Ti)O_3$ ultrathin films under open-circuit electrical boundary conditions, Physical review letters **106**, 196102 (2011).

[60] L. Lu, Y. Nahas, M. Liu, H. Du, Z. Jiang, S. Ren, D. Wang, L. Jin, S. Prokhorenko, C.-L. Jia, *et al.*, Topological defects with distinct dipole configurations in $PbTiO_3/SrTiO_3$ multilayer films, Physical review letters **120**, 177601 (2018).

[61] D. L. Andrews, *Structured light and its applications: An introduction to phase-structured beams and nanoscale optical forces* (Academic press, 2011).

[62] Z. Ji, W. Liu, S. Krylyuk, X. Fan, Z. Zhang, A. Pan, L. Feng, A. Davydov, and R. Agarwal, Photocurrent detection of the orbital angular momentum of light, Science **368**, 763 (2020).

[63] F. J. Belinfante, On the current and the density of the electric charge, the energy, the linear momentum and the angular momentum of arbitrary fields, Physica **7**, 449 (1940).

[64] A. Rusina, M. Durach, K. A. Nelson, and M. I. Stockman, Nanoconcentration of terahertz radiation in plasmonic waveguides, Optics express **16**, 18576 (2008).

[65] M. Schnell, P. Alonso-Gonzalez, L. Arzubiaga, F. Casanova, L. E. Hueso, A. Chuvilin, and R. Hillenbrand, Nanofocusing of mid-infrared energy with tapered transmission lines, Nature photonics **5**, 283 (2011).

[66] A. Toma, S. Tuccio, M. Prato, F. De Donato, A. Perucchi, P. Di Pietro, S. Marras, C. Liberale, R. Proietti Zaccaria, F. De Angelis, *et al.*, Squeezing terahertz light into nanovolumes: nanoantenna enhanced terahertz spectroscopy (nets) of semiconductor quantum dots, Nano letters **15**, 386 (2015).

[67] D. K. Gramotnev and S. I. Bozhevolnyi, Plasmonics beyond the diffraction limit, Nature photonics **4**, 83 (2010).

[68] L. Novotny and N. Van Hulst, Antennas for light, Nature photonics **5**, 83 (2011).

[69] R. W. Heeres and V. Zwiller, Subwavelength focusing of light with orbital angular momentum, Nano letters **14**, 4598 (2014).

[70] M. Pu, X. Ma, Z. Zhao, X. Li, Y. Wang, H. Gao, C. Hu, P. Gao, C. Wang, and X. Luo, Near-field collimation of light carrying orbital angular momentum with bull's-eye-assisted plasmonic coaxial waveguides, Scientific reports **5**, 1 (2015).

[71] D. Garoli, P. Zilio, Y. Gorodetski, F. Tantussi, and F. De Angelis, Optical vortex beam generator at nanoscale level, Scientific reports **6**, 1 (2016).

[72] G. Spektor, D. Kilbane, A. Mahro, B. Frank, S. Ristok, L. Gal, P. Kahl, D. Podbiel, S. Mathias, H. Giessen, *et al.*, Revealing the subfemtosecond dynamics of orbital angular momentum in nanoplasmonic vortices, Science **355**, 1187 (2017).

[73] J. A. Hachtel, S.-Y. Cho, R. B. Davidson, M. A. Feldman, M. F. Chisholm, R. F. Haglund, J. C. Idrobo, S. T. Pantelides, and B. J. Lawrie, Spatially and spectrally resolved orbital angular momentum interactions in plasmonic vortex generators, Light: Science & Applications **8**, 1 (2019).

[74] P. Genevet, N. Yu, F. Aieta, J. Lin, M. A. Kats, R. Blanchard, M. O. Scully, Z. Gaburro, and F. Capasso, Ultrathin plasmonic optical vortex plate based on phase discontinuities, Applied Physics Letters **100**, 013101 (2012).

[75] M. D. Williams, M. M. Coles, K. Saadi, D. S. Bradshaw, and D. L. Andrews, Optical vortex generation from molecular chromophore arrays, Physical review letters **111**, 153603 (2013).

[76] E. Karimi, S. A. Schulz, I. De Leon, H. Qassim, J. Upham, and R. W. Boyd, Generating optical orbital angular momentum at visible wavelengths using a plasmonic metasurface, Light: Science & Applications **3**, e167 (2014).

[77] Z. Jin, D. Janoschka, J. Deng, L. Ge, P. Dreher, B. Frank, G. Hu, J. Ni, Y. Yang, J. Li, *et al.*, Phyllotaxis-inspired nanosieves with multiplexed orbital angular momentum, ELight **1**, 1 (2021).

[78] B. Xu, J. Íñiguez, and L. Bellaiche, Designing lead-free antiferroelectrics for energy storage, Nature communications **8**, 1 (2017).

[79] Z. Jiang, Y. Nahas, S. Prokhorenko, S. Prosandeev, D. Wang, J. Íñiguez, and L. Bellaiche, Giant electrocaloric response in the prototypical $Pb(Mg, Nb)O_3$ relaxor ferroelectric from atomistic simulations, Physical Review B **97**, 104110 (2018).

[80] V. Garcia, S. Fusil, K. Bouzehouane, S. Enouz-Vedrenne, N. D. Mathur, A. Barthelemy, and M. Bibes, Giant tunnel electroresistance for non-destructive readout of ferroelectric states, Nature **460**, 81 (2009).

[81] A. Chanthbouala, A. Crassous, V. Garcia, K. Bouzehouane, S. Fusil, X. Moya, J. Allibe, B. Dlubak, J. Grollier, S. Xavier, *et al.*, Solid-state memories based on ferroelectric tunnel junctions, Nature nanotechnology **7**, 101 (2012).

[82] V. Garcia and M. Bibes, Ferroelectric tunnel junctions for information storage and processing, Nature communications **5**, 1 (2014).

[83] M. H. Kwak, S. B. Kang, K.-C. Kim, S. Y. Jeong, S. Kim, B. H. Yoo, D. C. Chung, H. C. Ryu, D. S. Jun, M. C. Paek, *et al.*, Dielectric characteristics of $Pb(Zr,Ti)O_3$ films on mgo single crystal substrate by terahertz time domain spectroscopy, Ferroelectrics **422**, 19 (2011).

[84] J. McPherson, J. Kim, A. Shanware, H. Mogul, and J. Rodriguez, Proposed universal relationship between dielectric breakdown and dielectric constant, in *Digest. International Electron Devices Meeting,* (IEEE, 2002) pp. 633–636.

[85] S. W. Ko, W. Zhu, C. Fragkiadakis, T. Borman, K. Wang, P. Mardilovich, and S. Trolier-McKinstry, Improvement of reliability and dielectric breakdown strength of nb-doped lead zirconate titanate films via microstructure control of seed, Journal of the American Ceramic Society **102**, 1211 (2019).

[86] I. Ponomareva and L. Bellaiche, Nature of dynamical coupling between polarization and strain in nanoscale ferroelectrics from first principles, Physical review letters **101**, 197602 (2008).

[87] P.-J. Hsu, A. Kubetzka, A. Finco, N. Romming, K. Von Bergmann, and R. Wiesendanger, Electric-field-

driven switching of individual magnetic skyrmions, Nature nanotechnology **12**, 123 (2017).

[88] J. Clark, L. Beitra, G. Xiong, A. Higginbotham, D. Fritz, H. Lemke, D. Zhu, M. Chollet, G. Williams, M. Messerschmidt, *et al.*, Ultrafast three-dimensional imaging of lattice dynamics in individual gold nanocrystals, Science **341**, 56 (2013).

[89] Y. Sheu, S. Trugman, L. Yan, Q. Jia, A. Taylor, and R. Prasankumar, Using ultrashort optical pulses to couple ferroelectric and ferromagnetic order in an oxide heterostructure, Nature Communications **5**, 5832 (2014).

[90] F. Chen, J. Goodfellow, S. Liu, I. Grinberg, M. C. Hoffmann, A. R. Damodaran, Y. Zhu, P. Zalden, X. Zhang, I. Takeuchi, *et al.*, Ultrafast terahertz gating of the polarization and giant nonlinear optical response in bifeo3 thin films, Advanced Materials **27**, 6371 (2015).

[91] F. Chen, Y. Zhu, S. Liu, Y. Qi, H. Hwang, N. C. Brandt, J. Lu, F. Quirin, H. Enquist, P. Zalden, *et al.*, Ultrafast terahertz-field-driven ionic response in ferroelectric BaTiO$_3$, Physical Review B **94**, 180104 (2016).

[92] H. Wen, M. J. Cherukara, and M. V. Holt, Time-resolved x-ray microscopy for materials science, Annual Review of Materials Research **49**, 389 (2019).

[93] Y. Zhang, J. Dai, X. Zhong, D. Zhang, G. Zhong, and J. Li, Probing ultrafast dynamics of ferroelectrics by time-resolved pump-probe spectroscopy, Advanced Science **8**, 2102488 (2021).

[94] M. Thomas, M. Brehm, R. Fligg, P. Vöhringer, and B. Kirchner, Computing vibrational spectra from ab initio molecular dynamics, Physical Chemistry Chemical Physics **15**, 6608 (2013).

[95] S. Chen, S. Yuan, Z. Hou, Y. Tang, J. Zhang, T. Wang, K. Li, W. Zhao, X. Liu, L. Chen, *et al.*, Recent progress on topological structures in ferroic thin films and heterostructures, Advanced materials **33**, 2000857 (2021).

[96] J. Junquera, Y. Nahas, S. Prokhorenko, L. Bellaiche, J. Íñiguez, D. G. Schlom, L.-Q. Chen, S. Salahuddin, D. A. Muller, L. W. Martin, *et al.*, Topological phases in polar oxide nanostructures, Reviews of Modern Physics **95**, 025001 (2023).

[97] O. I. Motrunich and A. Vishwanath, Emergent photons and transitions in the O(3) sigma model with hedgehog suppression, Physical Review B **70**, 075104 (2004).

[98] M.-h. Lau and C. Dasgupta, Numerical investigation of the role of topological defects in the three-dimensional heisenberg transition, Physical Review B **39**, 7212 (1989).